Catalysis Science & Technology

Nanosheet Assembled Microspheres Metal (Zn, Ni, and Cu) Indium Sulfides for highly Selective CO2 Electroreduction to Methane

Journal:	*Catalysis Science & Technology*
Manuscript ID	CY-ART-02-2024-000270.R1
Article Type:	Paper
Date Submitted by the Author:	25-Jun-2024
Complete List of Authors:	Ray, Schindra; North Carolina A&T State University, Chemistry Dahal, Rabin; North Carolina A&T State University, Chemistry Ashie, Mosses; North Carolina A&T State University, Chemistry Pathiraja, Gayani; University of North Carolina at Greensboro, Nanoscience; Bastakoti, Bishnu; North Carolina A&T State University, Chemistry

The authors declare that the data supporting this study are available within the main text and its supporting information. Should any raw data files be needed in another format, they are available from the corresponding author upon reasonable request.

ARTICLE

Nanosheet Assembled Microspheres Metal (Zn, Ni, and Cu) Indium Sulfides for highly Selective CO_2 Electroreduction to Methane

Received 00th January 20xx,
Accepted 00th January 20xx

DOI: 10.1039/x0xx00000x

Schindra Kumar Ray[a], Rabin Dahal[a], Moses D. Ashie[a], Gayani Pathiraja[b], Bishnu Prasad Bastakoti*[a]

Herein, metal indium sulfides ($ZnIn_2S_4$, $NiIn_2S_4$, and $CuInS_2$) were synthesized by hydrothermal method. Nanosheet-assembled microspheres were observed. According to cyclic voltammetry, $CuInS_2$ revealed 19 and 6-fold current density enhancement compared to $ZnIn_2S_4$ and $NiIn_2S_4$, respectively. Also, Linear sweep voltammetry results suggested a higher current density of $CuInS_2$ than others. The lowest Tafel plot of $CuInS_2$ (189.15 mV/dec) suggested the improvement of electrocatalytic activity than $ZnIn_2S_4$ (282.53 mV/dec) and $NiIn_2S_4$ (247.32 mV/dec). H-type cell was used for selective electrochemical reduction of CO_2 into CH_4. The gaseous and liquid products were analyzed by gas chromatography and ^1H NMR, respectively. Higher Faraday efficiencies (FEs) were observed in $CuInS_2$ (80.11%) than $ZnIn_2S_4$ (67.78%), $NiIn_2S_4$ (75.31%) towards the electrocatalytic reduction of CO_2 into methane (CH_4) at -0.6 V vs RHE. A higher turnover frequency (TOF) value was observed in $CuInS_2$ than in other catalysts. $CuInS_2$ demonstrated remarkable stability, with neither an obvious current drop nor large FEs fluctuation for 20 h during electrochemical CO_2 reduction into CH_4, indicating a superior electrocatalytic performance. The higher electrochemical performance of $CuInS_2$ is associated with a larger BET surface area/electrochemical surface area, rich structural design, and abundant active sites. This work indicates a promising strategy for developing a ternary electrocatalyst for highly selective electroreduction of CO_2 into CH_4.

Introduction

An increase in CO_2 emission levels to the atmosphere by the rapid depletion of fossil fuels has led to the energy crisis and global warming. Such problematic issues can be mitigated by converting CO_2 to value-added carbon-based fuels and chemical feedstock. Among various approaches, electrochemical CO_2 reduction is inexpensive, abundant, and environmentally friendly and can be performed under ambient temperature and pressure[1–4]. Electrochemical redox reaction consists of multiple proton/electron-transfer steps that can produce various types of C_1-C_3 gaseous or liquid products. Among different hydrocarbon products during electrochemical CO_2 reduction reaction (CO_2RR), methane (CH_4) is the most valuable C1 product because of its good compatibility with the current natural gas infrastructure[5]. In addition, the displacement of conventional CH_4 fuel production globally by the electrochemical CO_2RR technique can significantly contribute to a net zero CO_2 emissions economy. Unfortunately, electrocatalytic conversion of CO_2 into CH_4 suffers from slow kinetics *via* multiple electron transfer. Therefore, it is necessary to design an efficient electrocatalyst for selective electrocatalytic reduction of CO_2 into CH_4.

Nowadays, various electrocatalysts (nanotwinned Cu[5], Cu-MOF[6], Cu-porphyrin[7], C/Pt[8], Cu/CeO_2[9], and Zn atom[10] etc.) have been applied for selective electrochemical reduction of CO_2 into CH_4. However, precious metals, metal oxide, and MOF-based catalysts suffer from complicated synthesis processes, high cost, catalytic agglomeration, high rate of electrolysis[9], changes in active phases, element dissolution, and low electrochemical stability[1]. To solve these issues, ternary metal indium sulfide is a perfect option because the synergistic effect of metal and indium atoms facilitated greater affinity between cations in metal indium sulfide and CO_2 molecules and thus resulted in enhanced electrocatalytic performances[11]. Also, metal indium sulfide has excellent physical/chemical stability, is non-toxic, great durability, abundant metal vacancies, and In-S covalency that may greatly enhance the electrocatalytic performance [12–14]. In addition, metal tends to alter the coordination environment of indium sulfide, which may increase the electrocatalytic properties[14]. Among various metals, Zn, Ni, and Cu revealed superior electrochemical CO_2RR ability. These metals demonstrate the low-cost, well-defined structures, high surface to volume ratio, and great selectivity [6,15,16]

Recently, Cai et al. and Chi et al. fabricated $ZnIn_2S_4$ for electrocatalytic reduction of CO_2 into ethanol and formate, respectively[14,11]. However, electrocatalytic CO_2 reduction property of $NiIn_2S_4$ and $CuinS_2$ catalysts as well as selective electrocatalytic reduction of CO_2 into CH_4 have rarely been reported. Besides catalysts, good morphology can greatly promote electrocatalytic

[a] Department of Chemistry, North Carolina A & T State University, 1601 E Market St, Greensboro, NC 27411, USA.
[b] Department of Nanoscience, Joint School of Nanoscience & Nanoengineering, University of North Carolina at Greensboro, Greensboro, North Carolina 27401, USA

Electronic Supplementary Information (ESI) available: [SEM, BET,XRD, Electrochemical Characterization]

performances. Two dimensions (2D) nanosheet assembled microsphere not only provides the large surface area and prevents the aggregation of active sites but also lowers the contact resistance and thus enhances the electrocatalytic performances via efficient electron transfer[11]. Rich defects and abundant active sites nature of metal indium sulfide could lower the reaction barrier that can effectively reduce CO_2 to hydrocarbon electrocatalytically[17]. Also, sulphur sites of metal indium sulfide has low hydrogen absorption free energy that acts as a promotor to enhance hydrocarbon products[14]. So, nanosheet assembled microsphere catalysts ($ZnIn_2S_4$, $NiIn_2S_4$, and $CuInS_2$) are perfect options for selective electrocatalytic CO_2 reduction into CH_4.

In this work, $ZnIn_2S_4$, $NiIn_2S_4$, and $CuInS_2$ were synthesized by hydrothermal method. The catalysts were well characterized by various techniques. Various electrochemical measurements (cyclic voltammetry, electrochemical impedance spectroscopy, linear sweep voltammetry, Tafel. plot, and chronoamperometry) of $ZnIn_2S_4$, $NiIn_2S_4$, and $CuInS_2$ were carried on H-type cell. The stability of catalyst towards electrocatalytic CO_2RR for 20 h was performed. The gaseous and liquid products were investigated by gas chromatography (GC) and ^{1}H NMR, respectively. The Faradic efficiencies (FEs) towards selective reduction of CO_2 into CH_4 were calculated at -0.6 V vs RHE. Turnover frequency (TOF) was calculated for all catalysts. Possible mechanisms were explained.

Experimental Section

Materials

The chemicals used throughout all experiments consist of analytical grade and without any further purification. Zinc nitrate hexahydrate [$Zn(NO_3)_2.6H_2O$] (Alfa Aesar, LOT: R29E001, India), nickel (II) nitrate hexahydrate [$Ni(NO_3)_2.6H_2O$] (Honeywell, Lot No: 12220, US), copper (II) nitrate trihydrate [$Cu(NO_3)_2.3H_2O$] (Acros organics, Lot: A0412121, Poland), Indium(III) chloride tetrahydrate ($InCl_3.4H_2O$) (Sigma Aldrich, USA), and thioacetamide (TAA) (C_2H_5NS) (Sigma Aldrich, Switzerland) were used for the synthesis of catalysts. Potassium bicarbonate ($KHCO_3$) (Sigma Aldrich, Spain) was used as an electrolyte.

Synthesis of $ZnIn_2S_4$, $NiIn_2S_4$, and $CuInS_2$

Hydrothermal process was used to synthesize $ZnIn_2S_4$, $NiIn_2S_4$, and $CuInS_2$**.** In this process, 0.5×10^{-2} mole of $Zn(NO_3)_2.6H_2O$ was dissolved in 30 mL deionized water. In addition, 0.5×10^{-2} mole of $InCl_3.4H_2O$ and 10^{-2} mole of TAA were placed in 30 mL water. These solutions were magnetically stirred until the formation of a clear solution. Then, the resulting solutions were mixed and magnetically stirred for 4 h. After stirring, the suspension was transferred into a Teflon-lined stainless-steel autoclave with a capacity of 100 mL. Afterward, the autoclave was shielded and maintained at 180°/14 h. The obtained yellow precipitate was washed with water and ethanol several times. It was dried in an oven and $ZnIn_2S_4$ yellow powder was obtained. $Ni(NO_3)_2.6H_2O$ (0.5×10^{-2} mole) and $Cu(NO_3)_2.3H_2O$ (0.5×10^{-2} mole) were used to synthesize $NiIn_2S_4$ and $CuInS_2$ powders, respectively. These powders were used for further characterizations and electrochemical measurements. $ZnIn_2S_4$, $NiIn_2S_4$, and $CuInS_2$ were coded as ZIS, NIS, and CIS, respectively.

Material characterization

X-ray diffraction (XRD) patterns of sample was performed on a Rigaku Miniflex 600 (Japan) with Cu Kα radiation (2θ: 20 to 80°, continuous rate:4°/minute, and step: 0.02). The morphology of the samples was obtained by field emission scanning electron microscopy (FESEM, JEOL, JSM-IT800). The EDS elemental mapping/spectrum was obtained by Oxford instrument. Transmission electron microscopy (TEM), and high-resolution (HRTEM) image of sample was obtained from JEOL JEM-2100 plus at 120 kV. X-ray photoelectron spectroscopy (XPS) of the samples was measured on Thermo Scientific ESCALAB^{TM} XI (Al Kα and 200 eV). The Brunauer–Emmett–Teller (BET) surface area and pore size distribution of samples were obtained from NOVA 2200e (surface area and pore size analyzer). The analysis of gaseous products was identified by gas chromatography (GC) (SRI 8610C). Electrochemical characterizations were performed on CH instruments. The nuclear magnetic resonance (NMR) spectroscopy of liquid product was investigated on Ascend^{TM} 400, Bruker.

Electrochemical measurements

CH Instrument was used for measuring the electrochemical properties using a typical three-electrode system (counter electrode: platinum, reference electrode: Ag/AgCl, and working electrode: ZIS, NIS, and CIS). For electrolyte in electrochemical measurements, $KHCO_3$ (0.5 M) was used. For the preparation of working electrodes, 0.5 mL of C_2H_5OH, 50 μL nafion, and 4 mg of powder samples were mixed and sonicated for 4 h. As a substrate, FTO glass (MSE 2.2 mm, 12-15 ohm/sq, TEC 15 coated glass substrates), was washed with water/ethanol for 1 h under ultrasonication. It was dried at 70 °C for 4 h in a vacuum oven. The well-dispersed ink was put in glass substrate by controllable drop casting techniques. The available working area was 1 cm^2 in the glass electrode. Then, it was dried in an oven (70 °C/4 h).

CO_2 gas (99.999%) was continuously passed in the H-type cell for saturation of electrolyte for 40 min at 6 sccm. Mass flow controller (MC-100SCCM-D, Alicat Scientific) was used to regulate the flow rate of CO_2. To find the gaseous/liquid hydrocarbon products, GC was equipped with flame ionization detector (FID). For calibration, standard gas mixtures (ARC3) were applied under 1 atm and 298 K. Amperometry (*i-t)* measurements were performed at -0.6 V vs RHE. The injection of gas in GC was performed during electrochemical CO_2 RR. The concentration of gases in ppm was observed and Faradic efficiencies (FEs) were calculated. For electrocatalytic stability, the potential was applied at -0.6 V vs RHE for 20 h. In addition, turnover frequency (TOF) was calculated for all samples using following equation[18].

$$\text{TOF} = \frac{\text{Q}\times\text{FE}}{nF} \Big/ \frac{m\times \text{w}\%}{M\times \text{t}}$$

where Q, FE, F, n, m, w%, M, and t represent the total charge during chronoamperometry, Faradaic efficiency, Faraday constant, number of electrons exchanged for the CH_4 formation, mass of the materials loaded on working electrode, weight % of the catalyst from EDS, molecular weight of the materials, and time for the TOF unit, respectively.

Results and discussion

XRD diffraction spectra of the ZIS, NIS, and CIS samples were presented in **Fig. 1**. The XRD pattern of ZIS could be perfectly indexed to pure hexagonal phase of $ZnIn_2S_4$ (JCPDS No. 65-2023)[17,19] In addition, all diffraction peaks of NIS were matched with cubic spinel structure of $NiIn_2S_4$ (JCPDS No. 70-2900)[20,21]. Also, the tetragonal phase of $CuInS_2$ (JCPDS No. 85-1575) was found in the CIS sample [22,23]. Lack of impurity phase was observed in ZIS, NIS, and CIS samples successfully indicating fabrication of pure crystalline $ZnIn_2S_4$, $NiIn_2S_4$, and $CuInS_2$.

FESEM, TEM, and HRTEM images were performed to observe the morphologies and structures of the ZIS, NIS, and CIS (**Fig. 2 and Fig. 3**). According to **Fig. 2a**, the flower-like microspheres with a

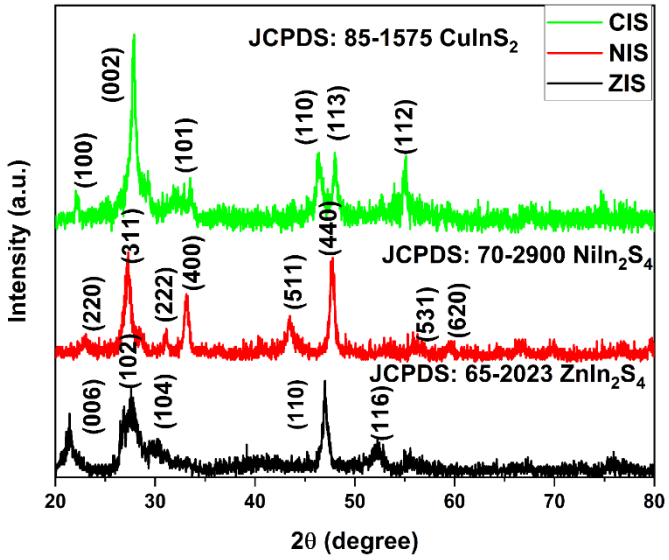

Fig.1. XRD patterns of ZIS, NIS, and CIS.

particle size of 2-10 μm were observed in ZIS particles which were composed of petal-like nanosheets. In addition, some hollow microspheres were clearly seen. NIS also revealed flower-like microspheres (2-7 μm) with a typical network structure/cavity containing various self-assembled nanosheet units (**Fig. 2b**). The microsphere of NIS was slightly distorted and agglomerated. A shown in **Fig. 2c**, microspheres (2 μm) were clearly observed. However, most of the microsphere were fused which were assembled with nanosheets. Various big cavities were clearly found as compared to ZIS and NIS. Such type of cavities along with interconnected nanosheet in microsphere facilitates the electron and electrolyte migration on the surface of the catalysts which is benefit for boosting the electrochemical performances towards the electrocatalytic CO_2RR. The possible reason for formation nanosheet assembled microsphere metal indium sulfide may associate with interaction of metal (Zn, Ni, and Cu) and In^{3+} cations as well as S^{2-} anions with H_2O. Due to this process, metal indium sulfide nuclei are produced. Also, excess TAA may attach with surface of newly formed crystal that can prevent the growth of crystal shape[24,25]. Then, metal indium sulfide nuclei grew into nanosheets and self-assembled to form flower-like microsphere which was driven by surface tension at high temperature during hydrothermal treatment[26]. Furthermore, FESEM elemental mapping and spectrum of ZIS, NIS, and CIS suggested the existence and uniform distribution of Zn, Ni, Cu, In, and S in the samples (**Fig. S1 and S2**).

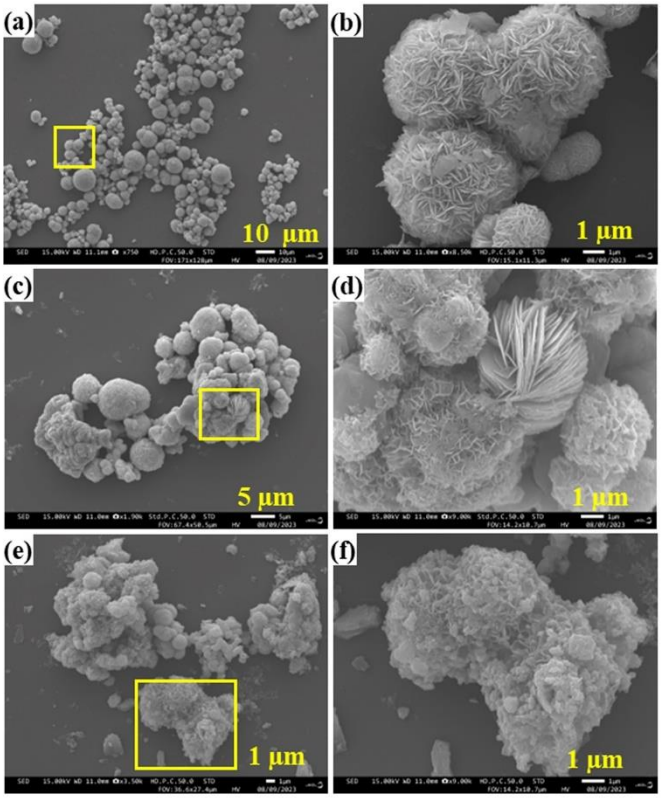

Fig. 2. FESEM images of ZIS (a and b), NIS (b and c), and CIS (d and e). The yellow-colored box indicates the magnified part.

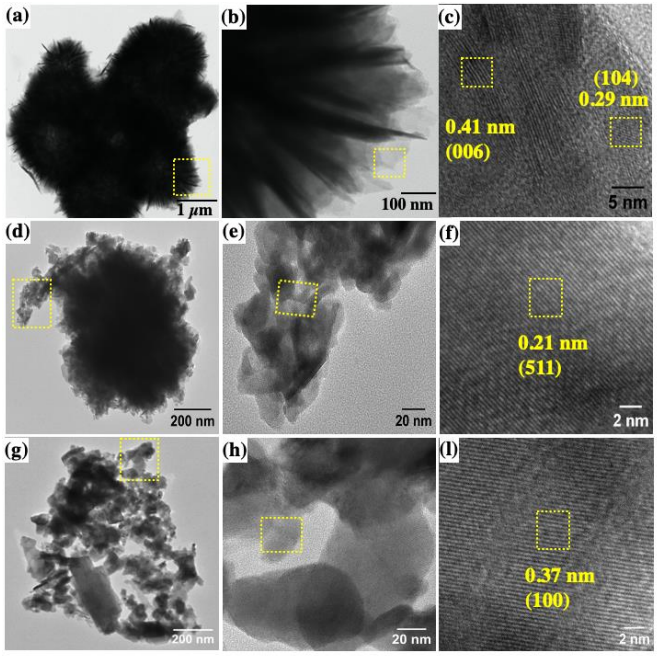

Fig. 3. TEM (ZIS: a and b, NIS: d and e, and CIS: g and h) and HRTEM (ZIS: c, NIS: f, and CIS: i). The yellow-colored dotted box indicates the magnified part.

The morphologies/structures of ZIS, NIS, and CIS were further investigated by TEM and HRTEM images (**Fig. 3**). TEM images suggested the microsphere composed of many nanosheets that was consistent with FESEM images. The magnified part of TEM images was shown in **Figs. 3b, 3e, and 3h**. The HRTEM image of ZIS showed the lattice spacing of 0.41 nm and 0.29 nm, corresponding to the (006) and (104) planes of $ZnIn_2S_4$, respectively (**Fig. 3c**). In addition, HRTEM images of NIS and CIS images indicate the spacing of the distinct lattice fringing with 0.21 nm and 0.37 nm, which can be indexed into the (511) and (100) planes of $NiIn_2S_4$ and $CuInS_2$, respectively (**Figs. 3f and 3i**). These planes were well matched with XRD patterns of samples suggesting the construction of pure $ZnIn_2S_4$, $NiIn_2S_4$, and $CuInS_2$ catalysts. **Fig. S3** presents the N_2 adsorption–desorption isotherms of ZIS, NIS, and CIS. All samples showed a type IV isotherm, that indicates nature of mesoporous materials. The surface area of ZIS, NIS, and CIS were 47.76, 253.32, and 280.48 m^2/g, respectively. CIS exhibited a higher surface area than others. Meanwhile, the pore-size distribution curves further verify the mesoporous structures in ZIS, NIS, and CIS (**Fig. S4)**. The mesopores were centred at 27-50 nm. So, the large surface area and porous structures could provide a large electrochemically active surface area on electrocatalysts for fast ions and charges transport as well as abundant surface active/adsorption sites that may enhance electrochemical CO_2RR[27,28].

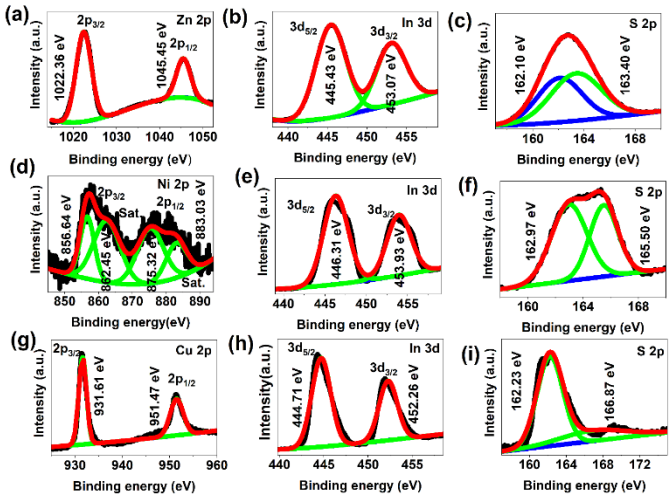

Fig. 4. XPS of ZIS (a: Zn 2p, b: In 3d, and c: S 2p), NIS (d: Ni 2p, e: In 3d, f: S 2p), and CIS (g; Cu 2p, h: In 3d, and i: S 2p).

To find the electronic chemical states of ZIS, NIS, and CIS, XPS was employed (**Fig. 4**). Zn 2p peaks centred at 1022.36 eV and 1045.45 eV which can be assigned to the $2p_{3/2}$ and $2p_{1/2}$ orbitals, respectively (**Fig. 4a**). As shown in **Fig. 4a**, the binding energy differences is about 23.09 eV that suggests the presence of Zn^{2+} in ZIS[13,29,30]. According to **Fig. 4d**, Ni $2p_{3/2}$ and Ni $2p_{1/2}$ peaks were located at 856.64 eV and 875.32 eV, respectively. In addition, satellite Ni $2p_{3/2}$ and Ni $2p_{1/2}$ peaks were observed at 862.45 eV and 883.03 eV, respectively. These results suggest the existence of Ni^{2+} in NIS[20,31–33]. Cu 2p core level was deconvoluted into two peaks representing Cu $2p_{3/2}$ (931.61 eV) and Cu $2p_{1/2}$ (951.47 eV), suggesting the valence state of ions is +1 in CIS (**Fig. 4g**)[34]. The In 3d spectra can be deconvoluted $3d_{5/2}$ (ZIS: 445.43 eV, NIS: 446.31 eV, CIS: 444.71 eV) and $3d_{3/2}$ signals (ZIS: 453.07 eV, NIS: 453.93 eV, CIS: 452.26 eV). This result suggests the presence of In^{3+} in samples (**Fig. 4b, 4e, and 4h**)[21]. The S 2p revealed $2p_{3/2}$ (ZIS: 162.10 eV, NIS: 162.97 eV, CIS: 162.23 eV) and $2p_{1/2}$ (ZIS: 163.40 eV, NIS: 165.50 eV eV, CIS: 166.87 eV) peaks indicating the formation of S^{2-} in the samples[13,35]. These XPS signals also provide evidence of metal (Zn, Ni, and Cu) sulfur bonds. Based on the above XPS analysis, it was confirmed that Zn^{2+}, Ni^{2+}, Cu^{+}, In^{3+}, and S^{2-} in the $ZnIn_2S_4$, $NiIn_2S_4$, and $CuInS_2$ catalysts.

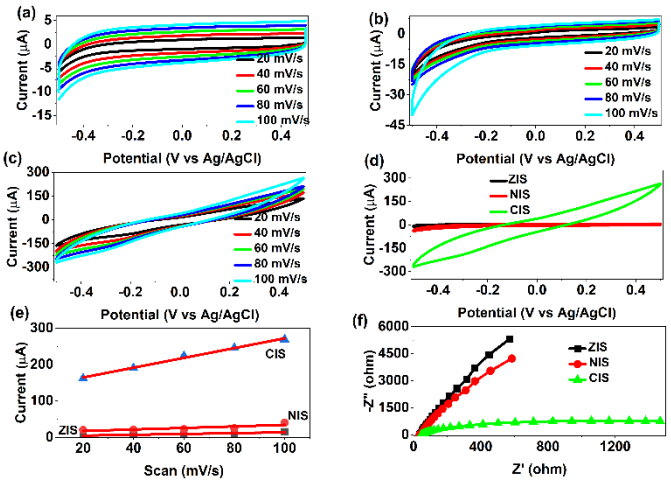

Fig. 5. CV (a) ZIS, (b) NIS, (c) CIS, and (d) combined plot at 100 mV/s scan rate), (e) plot of scan rare vs current, and (f) EIS.

The electrochemical activity of ZIS, NIS, and CIS was shown in **Fig. 5.** CV curve of electrocatalysts was performed at different scan rates (20, 40, 60, 80, 100 mV/S) within a potential window -0.5 to 0.5 (**Fig. 5a, 5b, 5c, and 5d)**. In the case of ZIS and NIS, CV curves were close to rectangular, and it revealed the feature of electric-double layer (EDL) capacitance (**Fig. 5a and 5b**). Such type of curves was usually obtained in porous structure that can suggest a continuous electron pathways and promote short ionic transmission distance for enhancement of electrochemical performances[36]. Sharp reduction peak was visible in CV curves. NIS showed a higher reduction potential/current densities/area than the ZIS. According to **Fig. 5c**, the non-ideal CV curves were obtained at all scan rates. Also, it deviated from rectangular shape that suggests the existence of both non-Faradic reaction/EDL and Faradaic reaction. It showed higher current densities than ZIS and NIS (**Fig. 5a-5d**). CIS showed 19 and 6-folds enhancement of current density than ZIS and NIS respectively indicating the higher electrocatalytic performances of $CuInS_2$ than $ZnIn_2S_4$ and $NiIn_2S_4$.

In all CV curves, current densities were increased with an increase in scan rate suggesting a good rate performance[37]. It may relate to the internal resistance catalysts and the polarization. The enhanced electrochemical performance of CIS than the ZIS and NIS might be associated with large surface area and superior pore size which can provide greater number of active sites for ion intercalation. The electrochemical surface area (ECSA) was obtained by double layer capacitance (C_{dl}) using various scan rates of electrocatalysts (**Fig. 5e**). The C_{dl} value of CIS is 1.35 mF cm^{-2} which is superior as compared to NIS (0.21 mF cm^{-2}) and ZIS (0.11 mF cm^{-2}) electrocatalyst. The exposure of more active sites provides great electrochemical performances of electrocatalyst. EIS plot was shown in **Fig. 5f**. According to Nyquist results, CIS presented more low impedance than ZIS and NIS. In addition, the equivalent circuit was designed *via* fitting the AC impedance spectrum (**Fig. S5**). Based on fitting, R1 (solution resistance), Warburg impedance coefficient (W), R2 (charge transfer resistance), constant phase element (Q), and double layer capacitance (F) were calculated (**Table S1**). CIS showed lower charge transfer resistance than ZIS and NIS suggesting a superior electrochemical performance via higher ion diffusion rate as well as great electron transport kinetics on electrode/electrolyte

interface.

Table 1. *Comparison of CH_4 conversion FEs of various electrocatalysts during electrocatalytic CO_2RR based on published literatures.*

Catalyst	**Synthesis method**	**Morphology**	**FEs -CH_4 (%)**	**Potential (V vs. RHE/SCE)**	**References**
Cu-CeO_2	Hydrothermal	Nanorod	49.3	-1.6	[38]
Ag-Cu_2O	Wet chemical reduction	Hollow nanosphere	62	-1.5	[39]
N-doped C/Cu	Calcination	Nanoparticles	30	-1.65	[40]
OH-AAn-COF-Cu	Shiff-base condensation	Nanofibers	77	-1	[41]
MWCNT-Por-COF-Cu	Mixing/heating/solvothermal	Nanotube	71.2	-0.7	[42]
Cu_2O/MOF	Electrochemical treatment	Nanoparticles	73	-1.4	[43]
Cu/MOF	Solvothermal	Rod	80	-0.9	[6]
Cu porphyrin	Chemical	Irregular	54.8	-1.63	[7]
Cu/CeO_2	Wet impregnation	Layered	15	-0.89	[9]
$ZnIn_2S_4$, $Niin_2S_4$, and $CuIns_2$	Hydrothermal	Nanosheet assembled microsphere	67.78, 75.31, and 80.11	-0.6	Our work

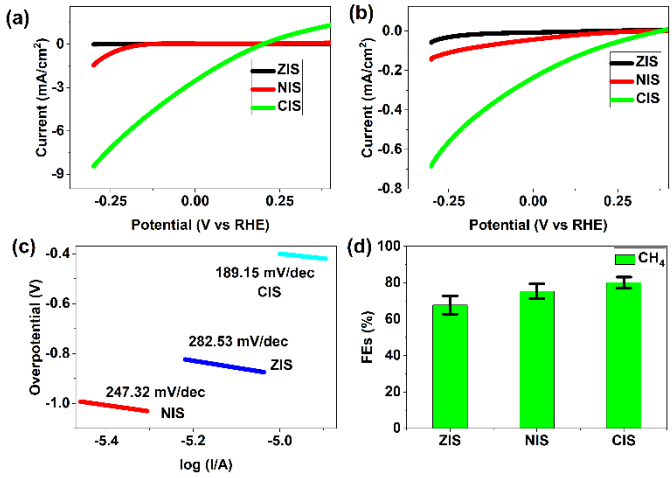

Fig. 6. LSV (a) before CO_2 saturated and (b) after CO_2 saturated), (c) Tafel plot, and (d) FEs at -0.6 V versus RHE of ZIS, NIS, and CIS.

To investigate the CO_2RR performances of electrocatalysts, LSV plots were evaluated. As shown in **Fig. 6a**, CIS showed higher current densities than ZIS and NIS at -0.3 V vs RHE. CIS demonstrated approximately five and four hundred fifty-folds enhancement of current density as compared to NIS and ZIS, respectively. The current density of ZIS, NIS, and CIS in CO_2-staurated 0.1 M $KHCO_3$ indicate higher current density of CIS than others **(Fig. 6b)**. It also suggests the excellent CO_2RR capability of $CuInS_2$ than $ZnIn_2S_4$ and $NiIn_2S_4$. Furthermore, CO_2RR conversion kinetics of electrocatalyst was further analysed by Tafel plots (**Fig. 6c**). The Tafel slops of ZIS, NIS, and CIS were found to be 282.53, 247.32, and 189.15 mV/dec, respectively. The lowest Tafel plot of CIS indicates the improvement of electrocatalytic activity compared to others. This result suggests that copper containing metal indium sulfide revealed higher electrocatalytic activity than Ni and Zn-based metal indium sulfide towards electrocatalytic CO_2RR.

To determine the reduction of CO_2 into hydrocarbon products electrocatalytically, steady-state current responses of ZIS, NIS, and CIS were evaluated in a CO_2-staurated electrolyte for 400 sec at -0.6 V vs RHE (**Fig. S6**). The current densities were -0.45 mA, 0.70 mA, and -1.69 mA for ZIS, NIS, and CIS, respectively. Gaseous and liquid products were obtained during the measurement of current densities at -0.6 V during electrocatalytic CO2RR. The gaseous products were observed by GC whereas liquid products were determined ^{1}H NMR (**Fig. S7 and Table S2**). As shown in **Fig. 6d**, FEs for ZIS, NIS, and CIS were 67.78%, 75.31%, and 80.11% towards CH_4 production during CO_2RR, respectively. The result suggests the selective reduction of CO_2 into CH_4 and superior FEs of $CuIn_2S_4$ compared to others during electrochemical reduction. The high electrocatalytic performance of CIS may be attributed to highly active BET surface area, electrochemical surface area, rich structural design, and good constraints on active species. In addition, liquid products were analysed by 1H NMR (Fig. S7). Two peaks (chemical shift-2.56: DMSO and 4.47: H2O) appeared in all samples that, indicate the absence of any liquid hydrocarbon products. Furthermore, TOF was calculated. TOF is one of a key parameter for CO_2RR efficiency evaluation. The TOF value of ZIS, NIS, and CIS (-0.6 V versus RHE for 400 sec) were 9.5×10^{-3} s^{-1}, 3.1×10^{-2} s^{-1}, and 0.171 s^{-1}, respectively. CIS revealed considerably higher TOF than NIS and ZIS suggesting superior electrocatalytic CO_2RR ability than others.

In addition, **Fig. S8** revealed the stability of $CuIn_2S_4$ for 20 h at -0.6 V vs RHE. Also, FEs were calculated after 20 h. The FEs of $CuIn_2S_4$ was 62.53% for CH_4 production during electrocatalytic reduction of CO_2 after 20 h (**Fig. S9**). The result revealed that Both FE and current density showed only minor decay over a 20 h period, suggesting significant electrochemical stability of CIS. It also showed evidence of stability towards the CH_4 generation. Further analyzing the XRD and FESEM images of CIS after the 20 h stability test, it could be found that phases and morphology were not changed, indicating the excellent stability of CIS (**Fig. S10-S11**). **Table 1** presents the comparison of FEs of different catalysts. This Table also indicates the comparable electrochemical CO_2RR performance of metal (Zn, Ni, and Cu) Indium Sulfides compared to other published literature.

According to mechanism related electrochemical CO_2RR, the structure/phase of the catalyst determines the adsorption and activation of CO_2 molecules[44]. Hexagonal, cubic, and tetragonal phases were observed in $ZnIn_2S_4$, $NiIn_2S_4$, and $CuInS_2$, respectively. (110) plane in metal indium sulfides may enhance the electron cloud between the metal (Zn, Ni, and Cu) atoms and S atoms that can provide electron donation from metals (M) to S atoms. Also, electrons may transfer from In to S atoms. The accumulation of charge around In to S or covalency in the catalyst determines the electrochemical CO_2RR performance[14]. The higher electrochemical CO_2RR ability of $CuInS_2$ may be associated with higher charge accumulation around In–S bonds[14,45]. Moreover, the interconnected nanosheet structure in the microsphere is beneficial to exposure of active sites for efficient CO_2RR[46].

In the case of metal sulfide-based catalysts, the single metal atom sites have tendency to generate weak bond with C or O atoms of adsorbed CO_2 *via* hybridization between 2p and 3d orbitals[47,48]. In addition, relatively weak bonds may form between metals M site with C or O (M site-C or M site-O) which can easily cleavage, and CO may be produced during electrochemical CO_2RR[49]. However, CH_4 was observed using metal (Zn, Ni, and Cu) indium sulfides during electrochemical CO_2RR. So, dual-metal active sites (In and M) in metal indium sulfides may be responsible for electrochemical CO_2RR to CH_4[49]. Dual-metal sites can provide high stable intermediate during the bonding of C and O atoms in the CO_2 molecules with two metal sites (Zn or Ni or Cu and In) *via* hybridization of 2p orbitals of C or O atoms and 3d orbitals of metal atoms. In this case, more energy is required to break the bond between metals and C or O for CO production. In addition, the protonation of C atoms may cause the weakening of the C-O and C-M bond strengths. Due to this reason, CH_4 was only observed during electrochemical CO_2RR of metal indium sulfides[49–52].

Based on CH_4 products during electrochemical CO_2RR by metal (Zn, Ni, and Cu) indium sulfides, the reaction pathways were proposed. At first, the protonation of *CO to *CHO is the potential

determining step as well as rate-determining step. The intermediate CO products is highly endergonic on metal indium sulfide catalysts that may cause the generation of CO is virtually prohibited. Also, hydrogen evolution may be prohibited. During this step, metal-indium dual sites may form stronger bonds with *CHO which can lower the energy barrier. Then, *CHO may produce *CH_3O species because of various proton−electron coupled reactions. In this step, the stronger metal-oxygen bond on the surface of metal indium sulfides may provide easier weakening and breakage of CH_3O group because of intense hybridization between the d-orbital of metal and the p-orbital of oxygen atoms. Also, introducing Cu, Ni, and Zn in metal indium sulfide may stabilize the *CH_3O intermediate and breakage of the C-O bond. Finally, CH_4 is produced on the surface of metal indium sulfide by breaking the C-O bond of *CH_3O[5,10,49,53,54].

Conclusions

In summary, nanosheet assembled metal indium sulfides ($ZnIn_2S_4$, $NiIn_2S_4$, and $CuInS_2$) were synthesized by hydrothermal method for selective electrochemical reduction of CO_2 into CH_4. The electrochemical characterization (CV, ESCA, EIS, LSV, chronoamperometry, and Tafel plot) of catalysts was performed that indicated the excellent electrochemical performances of $CuInS_2$ than $ZnIn_2S_4$ and $NiIn_2S_4$. The $CuInS_2$ exhibited a higher CH_4 FEs of 80.11% at −0.6 V vs RHE than other catalysts (ZnIn2S4: 67.78% and NiIn2S4: 75.31%) in an H-type cell. Also, $CuInS_2$ revealed higher TOF than others. The high selectivity for reducing CO_2 to CH_4 by metal indium sulfide electrocatalyst was attributed to great active sites, high BET surface area, excellent electrochemical surface area, and good structural design. Moreover, the catalyst demonstrated remarkable stability during the electrochemical reduction reaction for 20 h without lowering the current density. The stability of the catalyst was further supported by XRD and FESEM analysis after electrochemical CO_2RR. The possible mechanisms/pathways were proposed. This work may inspire new exploration and design of stable metal indium sulfide for highly selective electroreduction of CO_2 into CH_4.

Author Contributions

Schindra Kumar Ray: Conceptualization, Methodology, Validation, Formal analysis, Investigation, Data curation, Writing – original draft, review, and editing, **Rabin Dahal:** FESEM images, **Moses D. Ashie:** XPS measurement, **Gayani Pathiraja**: TEM images, **Bishnu Prasad Bastakoti:** Funding acquisition, Resources, Supervision, Writing- review & editing.

Conflicts of interest

There are no conflicts to declare.

Acknowledgements

The National Science Foundation's Excellence in Research Award (2100710) USA supported this research. Some of the characterizations were performed in the Joint School of Nanoscience and Nanoengineering, a member of the Southeastern Nanotechnology Infrastructure Corridor and National Nanotechnology Coordinated Infrastructure, which is supported by the National Science Foundation (Grant ECCS-1542174). The authors thank Professor Mufeed Basti for the BET measurement.

Notes and references

1 H. Wang, Y. K. Tzeng, Y. Ji, Y. Li, J. Li, X. Zheng, A. Yang, Y. Liu, Y. Gong, L. Cai, Y. Li, X. Zhang, W. Chen, B. Liu, H. Lu, N. A. Melosh, Z. X. Shen, K. Chan, T. Tan, S. Chu and Y. Cui, *Nat. Nanotechnol.*, 2020, **15**, 131–137.

2 S. K. Ray, R. Dahal, M. D. Ashie and B. P. Bastakoti, *Sci. Rep.*, 2024, **14**, 1406.

3 T. Zhang, H. Shang, B. Zhang, D. Yan and X. Xiang, *ACS Appl. Mater. Interfaces*, 2021, **13**, 16536–16544.

4 T. Gao, A. Kumar, Z. Shang, X. Duan, H. Wang, S. Wang, S. Ji, D. Yan, L. Luo, W. Liu and X. Sun, *Chinese Chem. Lett.*, 2019, **30**, 2274–2278.

5 J. Cai, Q. Zhao, W. Y. Hsu, C. Choi, Y. Liu, J. M. P. Martirez, C. Chen, J. Huang, E. A. Carter and Y. Huang, *J. Am. Chem. Soc.*, 2023, **145**, 9136–9143.

6 Y. Zhang, L. Z. Dong, S. Li, X. Huang, J. N. Chang, J. H. Wang, J. Zhou, S. L. Li and Y. Q. Lan, *Nat. Commun.*, 2021, **12**, 1–9.

7 P. Yu, X. Lv, Q. Wang, H. Huang, W. Weng, C. Peng, L. Zhang and G. Zheng, *Small*, 2023, **19**, 1–7.

8 M. Umeda, Y. Yoshida and S. Matsuda, *Electrochim. Acta*, 2020, **340**, 135945.

9 K. K. Patra, Z. Liu, H. Lee, S. Hong, H. Song, H. G. Abbas, Y. Kwon, S. Ringe and J. Oh, *ACS Catal.*, 2022, 10973–10983.

10 L. Han, S. Song, M. Liu, S. Yao, Z. Liang, H. Cheng, Z. Ren, W. Liu, R. Lin, G. Qi, X. Liu, Q. Wu, J. Luo, H. L. Xin, X. Liu, Q. Wu, J. Luo and H. L. Xin, *J. Am. Chem. Soc.*, 2020, **142**, 12563–12567.

11 F. Cai, X. Hu, F. Gou, Y. Chen, Y. Xu, C. Qi and D. K. Ma, *Appl. Surf. Sci.*, 2023, **611**, 155696.

12 G. Zhang, H. Wu, D. Chen, N. Li, Q. Xu, H. Li, J. He and J. Lu, *Green Energy Environ.*, 2022, 7, 176–204.

13 L. Wang, B. Cheng, L. Zhang and J. Yu, *Small*, 2021, **17**, 1–9.

14 L. P. Chi, Z. Z. Niu, X. L. Zhang, P. P. Yang, J. Liao, F. Y. Gao, Z. Z. Wu, K. Bin Tang and M. R. Gao, *Nat. Commun.*, 2021, **12**, 1–9.

15 L. Wu, L. Wu, C. Guo, Y. Guan, H. Wang and J. Lu, *Processes*, , DOI:10.3390/pr11041039.

16 S. He, D. Ji, J. Zhang, P. Novello, X. Li, Q. Zhang, X. Zhang and J. Liu, *J. Phys. Chem. B*, 2020, **124**, 511–518.

17 Y. He, H. Rao, K. Song, J. Li, Y. Yu, Y. Lou, C. Li, Y. Han, Z. Shi and S. Feng, *Adv. Funct. Mater.*, 2019, **29**, 1–10.

18 M. N. Hossain, P. Prslja, C. Flox, N. Muthuswamy, J. Sainio, A. M. Kannan, M. Suominen, N. Lopez and T. Kallio, *Appl. Catal. B Environ.*, 2022, **304**, 120863.

19 Z. Zhang, K. Liu, Z. Feng, Y. Bao and B. Dong, *Sci. Rep.*, 2016, **6**, 1–10.

20 J. Xia, Q. Wang, M. Wei, L. Chen, N. Liu, S. Fan and H. Wu, *J. Mater. Sci.*, 2021, **56**, 2372–2384.

21 A. Wang, H. Liang, F. Chen, X. Tian, S. Yin, S. Jing and P. Tsiakaras, *Appl. Catal. B Environ.*, 2022, **310**, 121336.

22 J. Ning, S. V. Kershaw and A. L. Rogach, *J. Am. Chem. Soc.*, 2019, **141**, 20516–20524.

23 D. Pan, L. An, Z. Sun, W. Hou, Y. Yang, Z. Yang and Y. Lu, *J. Am. Chem. Soc.*, 2008, **130**, 5620–5621.

24 X. Yin, B. Lv, Y. Kang, X. Xu, X. Lei, L. Li, H. Wang, H. Xi, J. Yang and Z. Yang, *Catal. Letters*, 2023, **153**, 570–583.

25 Z. Chen, D. Li, W. Zhang, C. Chen, W. Li, M. Sun, Y. He and X. Fu, *Inoragnic Chem.*, 2009, **40**, 9766–9772.
26 D. Wang, M. Cao, Y. Feng and J. Yao, *Microporous Mesoporous Mater.*, 2022, **330**, 111598.
27 S. Sun, H. Cheng, X. Li, X. Wu, D. Zhen, Y. Wang, R. Jin and G. He, *Ind. Eng. Chem. Res.*, 2021, **60**, 1164–1174.
28 S. K. Ray and B. P. Bastakoti, *Int. J. Hydrogen Energy*, 2024, **51**, 1109–1118.
29 S. K. Ray, D. Dhakal, J. Hur and S. W. Lee, *Nanotechnology*, , DOI:10.1088/1361-6528/ab53bf.
30 S. K. Ray, R. prasad Pandey, S. Jeong and S. Lee, *J. Photochem. Photobiol. A Chem.*, 2018, **367**, 162–170.
31 S. K. Ray, D. Dhakal, G. Gyawali, B. Joshi, A. Raj Koirala and S. W. Lee, *Chem. Eng. J.*, 2019, **373**, 259–274.
32 S. Kumar Ray, P. Anil Kumar Reddy, S. Yoon, J. Shin, K. Chon and S. Bae, *Chem. Eng. J.*, 2023, **452**, 139546.
33 M. A. Mushtaq, A. Kumar, G. Yasin, M. Tabish, M. Arif, S. Ajmal, W. Raza, S. Naseem, J. Zhao, P. Li, H. G. Ali, S. Ji and D. Yan, *Small*, 2024, **2310431**, 1–12.
34 X. Fu, J. Tao, Z. Zhao, S. Sun, L. Zhao, Z. He, Y. Gao and Y. Xia, *RSC Adv.*, 2023, **13**, 8227–8237.
35 M. A. Mushtaq, A. Kumar, G. Yasin, M. Arif, M. Tabish, S. Ibraheem, X. Cai, W. Ye, X. Fang, A. Saad, J. Zhao, S. Ji and D. Yan, *Appl. Catal. B Environ.*, 2022, **317**, 121711.
36 H. Guo, Z. Liu, H. Li, H. Wu, C. Zhang, J. Yang and X. Chen, *Appl. Phys. A Mater. Sci. Process.*, 2017, **123**, 1–9.
37 S. K. Ray and B. P. Bastakoti, *Int. J. Hydrogen Energy*, 2024, 51, 1109-1118.
38 L. Xue, C. Zhang, J. Wu, Q. Y. Fan, Y. Liu, Y. Wu, J. Li, H. Zhang, F. Liu and S. Zeng, *Appl. Catal. B Environ.*, 2022, **304**, 120951.
39 M. Sun, L. Zhang, F. Tian, J. Li, Y. Lei, H. Zhang, L. Han, Z. Guo, Y. Gao, F. Liu, Y. Wang, L. Wang and S. Zeng, *J. Energy Chem.*, 2024, **88**, 521–531.
40 C. J. Jiang, Y. Hou, H. Liu, L. T. Wang, G. R. Zhang, J. X. Lu and H. Wang, *J. Electroanal. Chem.*, 2022, **915**, 116353.
41 M. Liu, Y. R. Wang, H. M. Ding, M. Lu, G. K. Gao, L. Z. Dong, Q. Li, Y. Chen, S. L. Li and Y. Q. Lan, *Sci. Bull.*, 2021, **66**, 1659–1668.
42 H. Dong, M. Lu, Y. Wang, H. L. Tang, D. Wu, X. Sun and F. M. Zhang, *Appl. Catal. B Environ.*, 2022, 303, 120897.
43 J. Yi, R. Xie, Z. Xie, G. Chai, T. Liu, R. Chen, Y. Huang and R. Cao, *Angew. Chemie*, 2020, **132**, 23849–23856.
44 J. Yang, Z. Yang, K. Yang, Q. Yu, X. Zhu, H. Xu and H. Li, *Chinese J. Catal.*, 2023, **44**, 67–95.
45 W. Tao, C. Zhu, Q. Xu, S. Li, X. Xiong, H. Cheng, X. Zou and X. Lu, *ACS Omega*, 2020, **5**, 20090–20099.
46 J. Zhao, Z. Xiong, Y. Zhao, X. Chen and J. Zhang, *Environ. Res.*, 2023, **216**, 114699.
47 S. Wang, B. Y. Guan, Y. Lu and X. W. Lou, *J. Am. Chem. Soc.*, 2017, **139**, 17305–17308.
48 K. K. Ghuman, L. B. Hoch, P. Szymanski, J. Y. Y. Loh, N. P. Kherani, M. A. El-Sayed, G. A. Ozin and C. V. Singh, *J. Am. Chem. Soc.*, 2016, **138**, 1206–1214.
49 X. Li, Y. Sun, J. Xu, Y. Shao, J. Wu, X. Xu, Y. Pan, H. Ju, J. Zhu and Y. Xie, *Nat. Energy*, 2019, **4**, 690–699.
50 Y. Sun, S. Gao and Y. Xie, *Chem. Soc. Rev.*, 2014, **43**, 530–546.
51 S. Sorcar, J. Thompson, Y. Hwang, Y. H. Park, T. Majima, C. A. Grimes, J. R. Durrant and S. Il In, *Energy Environ. Sci.*, 2018, **11**, 3183–3193.
52 K. L. Bae, J. Kim, C. K. Lim, K. M. Nam and H. Song, *Nat. Commun.*, 2017, **8**, 1–8.
53 J. Zhao, P. Zhang, T. Yuan, D. Cheng, S. Zhen, H. Gao, T. Wang, Z. J. Zhao and J. Gong, *J. Am. Chem. Soc.*, 2023, **145**, 6622–6627.
54 Z. Sun, T. Ma, H. Tao, Q. Fan and B. Han, *Chem*, 2017, **3**, 560–587.